

# Passive Synthetic Aperture Hitchhiker Imaging of Ground Moving Targets—Part 2: Performance Analysis

Steven Wacks, *Student Member, IEEE*, and Birsen Yazıcı, *Senior Member, IEEE*

**Abstract**—In Part 1 of this paper, we present a passive synthetic aperture imaging and velocity estimation method for ground moving targets using a network of passive receivers. The method involves inversion of a Radon transform-type forward model via a novel filtered backprojection approach combined with entropy optimization. The method is applicable to non-cooperative transmitters of opportunity where the transmitter locations and transmitted waveforms are unknown. Furthermore, it can image multiple targets moving at different velocities in arbitrary imaging geometries. In this paper, we present a detailed analysis of the performance of our method. First the resolution analysis in position and velocity spaces is presented. The analysis identifies several factors that contribute positively or negatively toward position and velocity resolution. Next, we present a novel theory to analyze and predict smearing artifacts in position images due to error in velocity estimation of moving targets. Specifically, we show that small errors in the velocity estimation result in small positioning errors. We present extensive numerical simulations to demonstrate the theoretical results. While our primary interest lies in radar, the theory, methods, and algorithms introduced in this paper are also applicable to passive acoustic, seismic, and microwave imaging.

**Index Terms**—Synthetic aperture radar, passive imaging, passive radar, filtered backprojection, velocity estimation, resolution analysis, position error.

## I. INTRODUCTION

IN RECENT years, there has been growing interest in passive radar due to ever increasing radio frequency (RF) sources of opportunity, such as cell phone, TV, and radio broadcasting stations [1]–[11]. Additionally, passive radar systems are an attractive solution because of their inherent cost, simplicity, and stealth advantages. The problem of passive synthetic aperture imaging of moving targets is important, since targets of interest are often mobile. In Part 1 of this two-part study [12], we introduce a method of passive imaging of ground moving targets using a network of airborne receivers and non-cooperative transmitters of opportunity. In this paper,

we derive and analyze the performance of the imaging method that we introduced in Part 1. We present a resolution analysis on position and velocity and introduce a theory to analyze and predict smearing artifacts in the reconstructed position images due to incorrect velocity information. The investigation of achievable position and velocity resolution and error in target positioning due to velocity errors are important in designing and optimizing passive SAR imaging systems.

In Part 1, we present a novel forward model and an FBP-type image reconstruction combined with entropy optimization to reconstruct the radiance (position) images and to estimate 2D velocities of ground targets. The forward model is based on the correlation of the received signals from multiple moving receivers. We design a backprojection operator and analyze its point spread function. The analysis shows that when the velocity of a scatterer/target is correctly estimated, the backprojection puts the target at the correct position and orientation in the image. The filter is designed to get the strength of targets correctly. We reconstruct a stack of radiance images, each corresponding to a fixed, hypothesized velocity for a range of velocities. We analyze this stack of images using entropy as a measure of focus in order to estimate target velocities. The method is capable of imaging and estimating the velocities of multiple moving targets. While the method does not explicitly consider clutter, numerical simulations show that the entropy is a robust metric in estimating target velocities in relatively low signal-to-clutter ratios.

In Part 2 of this study, we examine the performance of the algorithm in two ways. First, we analyze the resolution of both target position and velocity estimation by looking at the bandwidth of range and spatial Doppler, respectively, available in the correlated data. Our analysis identifies several parameters related to transmitted waveforms and imaging geometry that contribute to position and velocity resolution. Next, we introduce a theory to analyze and predict smearing artifacts that appear in reconstructed radiance images due to the use of an incorrect hypothesized velocity in backprojection. The theory describes how velocity errors translate into positioning errors and the coupling between accurate target positioning and velocity estimation. We derive an analytic formula that relates the positioning errors/smearing caused by moving targets in images reconstructed using erroneous velocity information. This formula can be used for multiple purposes, both for the analysis and prediction of position errors arising from incorrectly hypothesized velocities, and understanding smearing artifacts in position images due

Manuscript received March 12, 2013; revised October 3, 2013, November 19, 2013, February 27, 2014, and June 5, 2014; accepted June 17, 2014. Date of publication July 8, 2014; date of current version August 18, 2014. This work was supported in part by the Air Force Office of Scientific Research under Grant FA9550-09-1-0013 and Grant FA9550-12-1-0415 and in part by the National Science Foundation under Grant CCF-08030672 and Grant CCF-1218805. The associate editor coordinating the review of this manuscript and approving it for publication was Prof. Jeffrey A. Fessler.

The authors are with the Department of Electrical, Computer and Systems Engineering, Rensselaer Polytechnic Institute, Troy, NY 12180 USA (e-mail: wackss@rpi.edu; yazici@ecse.rpi.edu).

Color versions of one or more of the figures in this paper are available online at <http://ieeexplore.ieee.org>.

Digital Object Identifier 10.1109/TIP.2014.2336543

to moving targets reconstructed under stationary scene assumption. Specifically, we also show that small errors in the velocity estimates results in small positioning errors in the reconstructed radiance images. Finally, we present extensive numerical simulations to demonstrate the performance of our method and to validate the theoretical results.

Section II reviews the forward model, image reconstruction, and velocity estimation algorithms from Part 1 of the study. Section III analyzes the position (radiance) resolution of the image reconstruction, assuming our hypothesized velocity is equal to the true velocity of the moving scene. Then, the velocity resolution is investigated by analyzing the potential velocity bandwidth available in the data. Section IV removes the assumption of a correctly hypothesized velocity and instead analyzes the nature of errors in target positioning due to an incorrect velocity. We present a theory and an analytic formula to show how the position and velocity errors are coupled. Numerical simulations are then presented in Section V. Finally, the paper is concluded in Section VI.

## II. OVERVIEW

This section briefly summarizes the forward model, radiance image reconstruction and velocity estimation methods described in Part 1 of this study to establish notation.

### A. Forward Model

In radar signal processing, a target is typically an object of interest in a scene that is being imaged. The term clutter is used for scattering objects that are not of interest. Note that we use the term scatterer for point targets. Thus, targets can be a composed of a single or multiple scatterers.

We denote the location of the scatters on the ground by  $\mathbf{x} = [\mathbf{x}, \psi(\mathbf{x})] \in \mathbb{R}^3$ , where  $\mathbf{x} = [x_1, x_2] \in \mathbb{R}^2$  and  $\psi$  is a known, smooth function for ground topography, i.e.,  $x_3 = \psi(\mathbf{x})$ . Since the targets are moving on the ground, the 3D velocity  $\mathbf{v}_\mathbf{x}$  of a moving scatterer located at  $\mathbf{x}$  at some reference time is given by  $\mathbf{v}_\mathbf{x} = [\mathbf{v}_\mathbf{x}, \nabla_\mathbf{x}\psi(\mathbf{x}) \cdot \mathbf{v}_\mathbf{x}]$  where  $\nabla_\mathbf{x}\psi(\mathbf{x})$  is the gradient of the ground topography.

We assume that there are  $N$  airborne receivers traversing trajectories  $\boldsymbol{\gamma}_i$ ,  $i = 1, \dots, N$  and a single transmitter of opportunity located at  $\mathbf{y}$ . Under the assumption that the range variation due to targets and receivers' movement within one pulse transmission and reception is negligible [13], the received signal can be modeled as

$$f_i(s, t) = \int e^{-i\omega[t - (|\mathbf{x} - \boldsymbol{\gamma}_i(s)| + |\mathbf{x} - \mathbf{y}|)/c_0]} e^{i\omega((\widehat{\mathbf{x} - \boldsymbol{\gamma}_i(s)} + \widehat{\mathbf{x} - \mathbf{y}}) \cdot \mathbf{v}_\mathbf{x} s)/c_0} \rho(\mathbf{x}) A_i(\omega, s, \mathbf{x}, \mathbf{v}) d\omega d\mathbf{x}, \quad (1)$$

where  $s$  denotes the slow-time or synthetic aperture sampling interval,  $t$  denotes fast-time,  $A_i$  is a slow-varying function of frequency  $\omega$  that depends on the transmitted waveform and geometric spreading factors, and  $\rho$  is the 2D ground reflectivity function at the beginning of the synthetic aperture  $s = 0$ .

We next cross-correlate the received signals  $f_i$ ,  $i = 1, \dots, N$  from different receivers and arrive at the forward model

$$d_{ij}(s, \tau) = \mathcal{F}[r](s, \tau), \quad i, j = 1, \dots, N, \quad i \neq j \\ = \int e^{-i\omega[\tau - R_{ij}(\mathbf{x}, s)/c_0 - B_{ij}(\mathbf{x}, \mathbf{v}, s)/c_0]} \\ \times A_{ij}(\omega, s, \mathbf{x}, \mathbf{v}) r(\mathbf{x}, \mathbf{v}) d\mathbf{v} d\mathbf{x} d\omega, \quad (2)$$

where  $d_{ij}$  denotes the cross-correlated received signal from the  $i$ th and  $j$ th receivers and  $\tau$  denotes *hitchhiker fast-time*, and

$$A_{ij}(\omega, s, \mathbf{x}, \mathbf{v}) = A_{R_{ij}}(\omega, s, \mathbf{x}, \mathbf{v}) \frac{R_T(\omega, \mathbf{x})}{(4\pi)^2 |\mathbf{x} + \mathbf{v}_\mathbf{x} s - \mathbf{y}|^2}, \quad (3)$$

$$R_{ij}(\mathbf{x}, s) = |\mathbf{x} - \boldsymbol{\gamma}_i(s)| - |\mathbf{x} - \boldsymbol{\gamma}_j(s)|, \quad (4)$$

$$B_{ij}(\mathbf{x}, s) = [(\widehat{\mathbf{x} - \boldsymbol{\gamma}_i(s)}) - (\widehat{\mathbf{x} - \boldsymbol{\gamma}_j(s)})] \cdot \mathbf{v}_\mathbf{x}, \quad (5)$$

where  $\widehat{\mathbf{x}}$  denotes the unit vector in the direction of  $\mathbf{x}$ .

$A_{ij}$  is a slow-varying function of  $\omega$  satisfying the assumption (17) in [12].  $r(\mathbf{x}, \mathbf{v})$  is the phase-space radiance function defined by  $r(\mathbf{x}, \mathbf{v}) \approx R_\rho(\mathbf{x})\varphi(\mathbf{v}, \mathbf{v}_\mathbf{x})$  where  $R_\rho$  is the 2D scene radiance and  $\varphi(\mathbf{v}, \mathbf{v}_\mathbf{x})$  is a smooth function of  $\mathbf{v}$  that approximates  $\delta(\mathbf{v} - \mathbf{v}_\mathbf{x})$ .

Let

$$\varphi_{ij}(\mathbf{x}, \mathbf{v}, s) = R_{ij}(\mathbf{x}, s) + B_{ij}(\mathbf{x}, \mathbf{v}, s). \quad (6)$$

Then, the phase of  $\mathcal{F}$  is

$$\omega[\tau - \frac{1}{c_0}\varphi_{ij}(\mathbf{x}, \mathbf{v}, s)] \quad (7)$$

and its amplitude is  $A_{ij}$ .

### B. Image Formation

For a given hypothesized velocity  $\mathbf{v}_h$ , we form a position image via the following filtered backprojection operator:

$$\mathcal{K}[d_{ij}](\mathbf{x}') = \hat{r}_{ij}^{\mathbf{v}_h}(\mathbf{x}') \\ = \int e^{i\omega[\tau - R_{ij}(\mathbf{x}', s)/c_0 - B_{ij}(\mathbf{x}', \mathbf{v}_h, s)/c_0]} \\ \times d_{ij}(s, \tau) Q_{ij}^{\mathbf{v}_h}(\omega, s, \mathbf{x}') d\omega ds d\tau \quad (8)$$

where  $Q_{ij}$  is the filter that varies slowly with  $\omega$  derived in [12].

The final image is formed by coherently summing over all pairs of images:

$$\hat{r}^{\mathbf{v}_h}(\mathbf{x}') = \sum_{i,j} \hat{r}_{ij}^{\mathbf{v}_h}(\mathbf{x}'). \quad (9)$$

Note that under the assumption that  $A_{ij}$  and  $Q_{ij}$  are slow-varying functions of  $\omega$ , both  $\mathcal{F}$  and  $\mathcal{K}$  become Fourier Integral Operators (FIO).

The point spread function (PSF) analysis in [12] shows that irrespective of the choice of  $Q_{ij}$ , the backprojection operator positions the scatterer located at  $\mathbf{x}$  in the scene correctly in the reconstructed image whenever  $\mathbf{v}_h = \mathbf{v}_\mathbf{x}$ . Additionally, we design the filter  $Q_{ij}$  so that the PSF function is approximately  $\delta(\mathbf{x} - \mathbf{x}')$  whenever  $\mathbf{v}_h = \mathbf{v}_\mathbf{x}$ . This filter is found to be

$$Q_{ij}(\boldsymbol{\xi}_{ij}, \mathbf{x}', \mathbf{v}_h) = \frac{\chi\Omega A_{ij}^*(\boldsymbol{\xi}_{ij}, \mathbf{x}', \mathbf{v}_h) |\omega|}{|A_{ij}(\boldsymbol{\xi}_{ij}, \mathbf{x}', \mathbf{v}_h)|^2 c_0^2} \\ \times |\Xi_{ij,1} \dot{\Xi}_{ij,2} - \Xi_{ij,2} \dot{\Xi}_{ij,1}|, \quad (10)$$

where  $\Xi_{ij} = [\Xi_{ij,1}, \Xi_{ij,2}]$ , with

$$\Xi_{ij}(s, \mathbf{x}', \mathbf{v}) = \nabla_{\mathbf{x}}[-R_{ij}(\mathbf{x}, s) - B_{ij}(\mathbf{x}, \mathbf{v}, s)]|_{\mathbf{x}=\mathbf{x}'} \quad (11)$$

and

$$\xi_{ij} = \frac{\omega}{c_0} \Xi_{ij}(s, \mathbf{x}', \mathbf{v}). \quad (12)$$

$\chi_{\Omega}$  is a smooth cut-off function to prevent division by zero,  $\Omega$  is the set of points  $\mathbf{x}'$  where  $A_{ij}(\omega, s, \mathbf{x}, \mathbf{v}) \neq 0$  and  $A_{ij}^*$  denotes the complex conjugate of  $A_{ij}$ .

### C. Velocity Estimation Algorithm

To estimate the velocity of the moving targets, a stack of images is formed by filtering and backprojecting the correlated data over a range of hypothesized velocities. Minimum entropy is then used as a measure of focus for each image. Entropy is computed for each image by

$$\text{En}(v_h) = - \sum_{\mathbf{x}'} p(\hat{r}(\mathbf{x}', v_h)) \log[p(\hat{r}(\mathbf{x}', v_h))], \quad (13)$$

where  $p$  is a normalized histogram for the discrete image. Since moving targets are focused more sharply when their hypothesized velocity is correct, target velocities are determined by the local minima of  $\text{En}$  over the range of hypothesized velocities.

In the following two sections, we analyze position and velocity resolutions and the positioning errors due to incorrect estimation of target velocities.

## III. RESOLUTION ANALYSIS

This section analyzes the resolution in the available data for both position and velocity. This tells us which factors are important to focus on for increasing the resolution in each of these dimensions, allowing for more accurate image reconstruction and velocity estimation. First, we study the resolution in reconstructing a position image for the correct hypothesized velocity. Afterward, the velocity resolution available in the data is analyzed.

### A. Resolution of Reconstructed Position Images

To analyze the resolution of the reconstructed images, we analyze the bandwidth of the point spread function. Recall that the PSF of the imaging operator  $\mathcal{K}$  is the kernel of the image fidelity operator  $\mathcal{KF}$ . When the hypothesized velocity  $v_h$  is equal to the correct velocity  $v_x$  and the filter  $Q_{ij}$  is chosen as in (10), for a given pair of receivers this kernel is approximated by

$$L_{ij}^{(v_h, v_h)}(\mathbf{x}, \mathbf{x}') = \int_{\Omega_{ij}} e^{i(\mathbf{x}-\mathbf{x}') \cdot \xi_{ij}} d\xi_{ij}, \quad (14)$$

where

$$\Omega_{ij} = \{\xi_{ij} : \xi_{ij} = \frac{\omega}{c_0} \Xi_{ij}(s, \mathbf{x}', v_h), \mathbf{x}' \in \text{supp}(A_{ij} Q_{ij}^{v_h})\}. \quad (15)$$

The point spread function shows that the reconstructed image is a band-limited version of the original image, with a bandwidth determined by the data collection manifold,  $\Omega_{ij}$ . Alternatively, we can interpret the vector  $\xi_{ij}$  as the Fourier

vector that contributes to the reconstruction of the pixel at  $\mathbf{x}'$ . Thus, to obtain good resolution at  $\mathbf{x}'$ , it is desirable for this vector to span a wide range of angles and have a large magnitude. The bandwidth contribution of  $\xi_{ij}$  to the reconstructed image is

$$\xi_{ij} = \frac{\omega}{c_0} \left[ D\psi(\mathbf{x}')[(\mathbf{x}' - \widehat{\boldsymbol{\gamma}}_i(s)) - (\mathbf{x}' - \widehat{\boldsymbol{\gamma}}_j(s))] - \frac{D\psi(\mathbf{x}') \cdot \mathbf{v}_i^{\perp} s + \partial_{\mathbf{x}'}^2 \psi(\mathbf{x}') \cdot \mathbf{v}(\psi(\mathbf{x}') - \boldsymbol{\gamma}_i^3(s))s}{|\mathbf{x}' - \boldsymbol{\gamma}_i(s)|} + \frac{D\psi(\mathbf{x}') \cdot \mathbf{v}_j^{\perp} s + \partial_{\mathbf{x}'}^2 \psi(\mathbf{x}') \cdot \mathbf{v}(\psi(\mathbf{x}') - \boldsymbol{\gamma}_j^3(s))s}{|\mathbf{x}' - \boldsymbol{\gamma}_j(s)|} \right], \quad (16)$$

where

$$D\psi(\mathbf{x}) = \begin{bmatrix} 1 & 0 & \partial\psi(\mathbf{x})/\partial x_1 \\ 0 & 1 & \partial\psi(\mathbf{x})/\partial x_2 \end{bmatrix}, \quad (17)$$

and

$$\mathbf{v}_i^{\perp} = \mathbf{v} - (\mathbf{x} - \widehat{\boldsymbol{\gamma}}_i(s))[(\mathbf{x} - \widehat{\boldsymbol{\gamma}}_i(s)) \cdot \mathbf{v}], \quad (18)$$

$$\mathbf{v}_j^{\perp} = \mathbf{v} - (\mathbf{x} - \widehat{\boldsymbol{\gamma}}_j(s))[(\mathbf{x} - \widehat{\boldsymbol{\gamma}}_j(s)) \cdot \mathbf{v}]. \quad (19)$$

The  $D\psi(\mathbf{x})$  matrix projects a 3D vector onto the tangent plane of the ground topography. Note that  $\mathbf{v}_i^{\perp}$  represents the component of the target velocity in the direction perpendicular to the look direction,  $(\mathbf{x} - \widehat{\boldsymbol{\gamma}}_i(s))$  of the  $i$ th receiver.

For flat topography, (16) simplifies to

$$\xi_{ij} = \frac{\omega}{c_0} D\psi(\mathbf{x}') \left[ [(\mathbf{x}' - \widehat{\boldsymbol{\gamma}}_i(s)) - (\mathbf{x}' - \widehat{\boldsymbol{\gamma}}_j(s))] + \frac{\mathbf{v}_j^{\perp} s}{|\mathbf{x}' - \boldsymbol{\gamma}_j(s)|} - \frac{\mathbf{v}_i^{\perp} s}{|\mathbf{x}' - \boldsymbol{\gamma}_i(s)|} \right], \quad (20)$$

where

$$D\psi(\mathbf{x}) = \begin{bmatrix} 1 & 0 & 0 \\ 0 & 1 & 0 \end{bmatrix}. \quad (21)$$

From this equation we can make conclusions about the resolution of the reconstructed image. First, we see that the bandwidth of the transmitted waveform,  $f = \omega/2\pi$ , directly contributes to the magnitude of  $\xi_{ij}$ , and increasing this parameter yields a corresponding increase in reconstructed image resolution.

If we assume a stationary scene, the two  $\mathbf{v}^{\perp}$  terms vanish and we are left with the hitchhiker look direction, which is the difference in antenna look directions  $(\mathbf{x}' - \widehat{\boldsymbol{\gamma}}_i(s)) - (\mathbf{x}' - \widehat{\boldsymbol{\gamma}}_j(s))$  projected onto the tangent plane of the ground topography. The magnitude of this term is proportional to the hitchhiker angle  $\theta_h$ , which is the angle between these 3D vectors:

$$|(\mathbf{x}' - \widehat{\boldsymbol{\gamma}}_i(s)) - (\mathbf{x}' - \widehat{\boldsymbol{\gamma}}_j(s))| = 2|\sin(\theta_h/2)|. \quad (22)$$

This angle is depicted in Fig. 1. When this angle is small the antennas are close together, and this term will approach zero. For the best resolution, the sine function should be maximized by forcing  $\theta_h = 180^\circ$ , i.e., a larger the hitchhiker angle increases the position resolution.

Additionally, the bandwidth contribution of  $\xi_{ij}$  to the reconstructed image is affected by the target velocities.

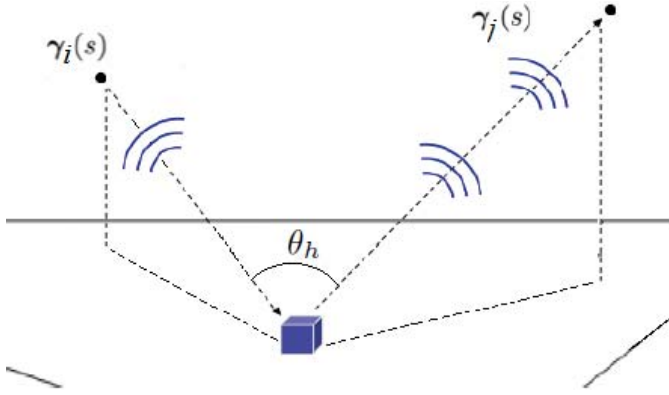


Fig. 1. Hitchhiker angle  $\theta_h$ , the angle between the antenna look-direction vectors.

To understand the contribution of the velocity of moving targets to position resolution, we decompose  $\xi_{ij}$  into two components

$$\mathbf{L}_{ij} = \mathbf{L}_{ij}(\mathbf{x}', s) = (\mathbf{x}' - \widehat{\boldsymbol{\gamma}}_i(s)) - (\mathbf{x}' - \widehat{\boldsymbol{\gamma}}_j(s)), \quad (23)$$

$$\mathbf{V}_{ij} = \mathbf{V}_{ij}(\mathbf{x}', \mathbf{v}, s) = \frac{\mathbf{v}_j^\perp s}{|\mathbf{x}' - \boldsymbol{\gamma}_j(s)|} - \frac{\mathbf{v}_i^\perp s}{|\mathbf{x}' - \boldsymbol{\gamma}_i(s)|}, \quad (24)$$

where (23) denotes the hitchhiker look direction and (24) defines the velocity components of  $\xi_{ij}$  given in (20). Assuming that  $|\mathbf{v}_i^\perp s| \ll |\mathbf{x}' - \boldsymbol{\gamma}_i(s)|$  for all  $i$ , we make the following approximation

$$|\mathbf{L}_{ij} + \mathbf{V}_{ij}| \approx |\mathbf{L}_{ij}| + \hat{\mathbf{L}}_{ij} \cdot \mathbf{V}_{ij}. \quad (25)$$

From this equation, we see that the bandwidth contribution is proportional to the component of the velocity term in the hitchhiker look direction.  $\mathbf{v}_i^\perp$  is orthogonal to the look direction of antenna  $i$  and  $\mathbf{v}_j^\perp$  is orthogonal to the look direction of antenna  $j$ , i.e.,

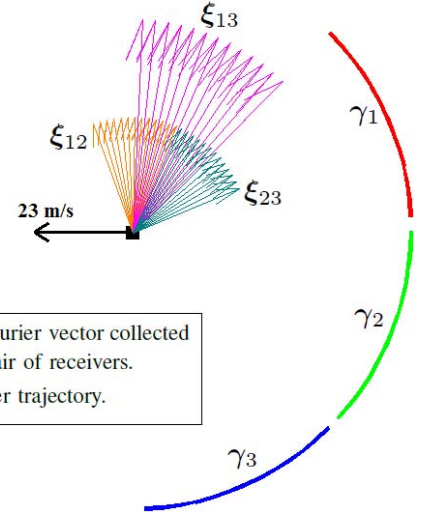
$$(\mathbf{x}' - \widehat{\boldsymbol{\gamma}}_i(s)) \cdot \mathbf{v}_i^\perp = 0, \quad (26)$$

$$(\mathbf{x}' - \widehat{\boldsymbol{\gamma}}_j(s)) \cdot \mathbf{v}_j^\perp = 0. \quad (27)$$

Therefore, the dot product simplifies to

$$\begin{aligned} & \hat{\mathbf{L}}_{ij} \cdot \mathbf{V}_{ij} \\ &= \frac{1}{|\mathbf{L}_{ij}|} \left[ \frac{(\mathbf{x}' - \widehat{\boldsymbol{\gamma}}_i(s)) \cdot \mathbf{v}_j^\perp s}{|\mathbf{x}' - \boldsymbol{\gamma}_j(s)|} + \frac{(\mathbf{x}' - \widehat{\boldsymbol{\gamma}}_j(s)) \cdot \mathbf{v}_i^\perp s}{|\mathbf{x}' - \boldsymbol{\gamma}_i(s)|} \right] \\ &= \frac{|\mathbf{v}|}{2|\sin(\theta_h/2)|} \left[ \frac{\sin(\theta_j) \cos(\theta_i^{j\perp}) s}{|\mathbf{x}' - \boldsymbol{\gamma}_j(s)|} + \frac{\sin(\theta_i) \cos(\theta_j^{i\perp}) s}{|\mathbf{x}' - \boldsymbol{\gamma}_i(s)|} \right] \end{aligned} \quad (28)$$

where  $\theta_i$  and  $\theta_j$  are the angles between the velocity vector and look directions of antennas  $i$  and  $j$ , respectively. We see that the sine of the hitchhiker angle is present in the denominator in this term. However, since this term is generally much smaller than  $\mathbf{L}_{ij}$ , the overall resolution is still improved with a larger hitchhiker angle. The angle  $\theta_i^{j\perp}$  is the angle between the antenna  $i$  look direction and the component velocity perpendicular to antenna  $j$ . In this expression, the distances between the scene and each of the receivers,  $|\mathbf{x}' - \boldsymbol{\gamma}_i(s)|$  and



$\xi_{ij}$ : spatial Fourier vector collected by  $ij^{\text{th}}$  pair of receivers.  
 $\boldsymbol{\gamma}_i$ :  $i^{\text{th}}$  receiver trajectory.

Fig. 2. Data collection manifold  $\Omega_{ij}$ , i.e. set of spatial Fourier vectors,  $\xi_{ij}$  for  $i, j = 1, 2, 3$ , collected by three pairs of receivers over a range of slow-time values for a point target moving with velocity 23 m/s towards the left. Each receiver is separated by  $45^\circ$  and traversing  $45^\circ$  of a circular aperture. Clearly, each pair of receivers increases the angular span of Fourier vectors for a fixed coherent processing interval.

$|\mathbf{x}' - \boldsymbol{\gamma}_j(s)|$ , are negatively correlated with the magnitude of  $\xi_{ij}$ . Therefore, the closer the antennas are to the scene of interest, the better the resulting image resolution. In addition, the magnitude is also directly proportional to the magnitude  $|\mathbf{v}|$ , so the resolution also increases with the speed of the moving target. The angles between the velocity-related vectors and antenna look directions play the largest role when the antennas are far apart, at approximately a hitchhiker angle of  $90^\circ$ . For example, in this scenario, the  $\mathbf{v}_j^\perp$  vector will be mostly aligned with the antenna  $i$  look direction. Finally, the  $\mathbf{v}^\perp$  vectors themselves will be largest when the velocity vectors are perpendicular to the antenna look directions where there is a large tangential velocity component.

High image resolution also requires a wide angular diversity in  $\xi_{ij}$  vectors. The direction of  $\xi_{ij}$  is determined largely by the hitchhiker look direction. The angular span of the  $\xi_{ij}$  vectors in the data collection manifold is determined by the “effective” length of the aperture. Assuming that appropriate flight trajectories are chosen, the aperture length is directly proportional to the length of  $s$  and the number of receiver pairs. Fig. 2 shows the set of Fourier vectors,  $\xi_{ij}$ ,  $i, j = 1, 2, 3$  obtained by three receivers each traversing a  $45^\circ$  arc over a circular aperture in tandem for a set of slow-time values. We see that each pair of receivers collects  $\xi_{ij}$  vectors spanning a different range of directions for the same set of slow-time values. The angular range of the Fourier vectors for each pair depends on the length of slow-time and the magnitude of the Fourier vectors depends on the hitchhiker look-direction for a fixed bandwidth. Clearly, increasing the number of receivers increases the angular span of the Fourier vectors for a fixed coherent processing interval (CPI). Hence a large number of receivers can be used to collect high resolution information in a relatively short CPI. This may be advantageous in imaging fast maneuvering targets.

TABLE I  
TABLE OF IMAGE RESOLUTION PARAMETERS

Parameter	Increase ( $\uparrow$ )	Resolution
Signal bandwidth $f = \omega/2\pi$	$\uparrow$	$\uparrow$
Hitchhiker angle $\sin(\theta_h/2)$	$\uparrow$	$\uparrow$
Distance $ \mathbf{x}' - \boldsymbol{\gamma}_i(s) ,  \mathbf{x}' - \boldsymbol{\gamma}_j(s) $	$\uparrow$	$\downarrow$
Target speed $ \mathbf{v} $	$\uparrow$	$\uparrow$
Angles between antenna look direction and target velocity $\theta_i, \theta_j$	$\uparrow$	$\uparrow$
Aperture length $s$	$\uparrow$	$\uparrow$
Number of receivers	$\uparrow$	$\uparrow$

Table I summarizes these conclusions. Under most conditions, the stationary term will dominate, since the velocity component is normalized by the antenna ranges. The dominating parameters here are represented in the first part of the table above the horizontal line. However, when this stationary term becomes small it can still be affected by the velocity component. These parameters are shown in the second part of the table.

### B. Resolution Analysis for a Simplified Imaging Geometry

We assume a stationary receiver located at  $\boldsymbol{\gamma}_1(s) = [0, 0, h]$  and a moving receiver located at  $\boldsymbol{\gamma}_2(s) = [0, s, h]$ , where  $h$  is the height of both receivers and  $s \in [-s_1, s_1]$ .

The kernel of the image fidelity operator, the point spread function, contains the resolution information, and is of the form

$$K(\mathbf{x}, \mathbf{z}) = \int_{\Omega_{\mathbf{z}}} e^{i(\mathbf{x}-\mathbf{z}) \cdot \boldsymbol{\xi}} d\boldsymbol{\xi}, \quad (29)$$

where the limits of integration is determined by the data collection manifold  $\Omega_{\mathbf{z}}$ . The  $\boldsymbol{\xi}$  vector for a flat ground topography is given in (20)-(21). Since the distance travelled by a target is typically much smaller than the range of the antennas, for the rest of our analysis, we assume that

$$\boldsymbol{\xi} \approx \frac{\omega}{c_0} D\psi[(\mathbf{x} - \widehat{\boldsymbol{\gamma}}_1(s)) - (\mathbf{x} - \widehat{\boldsymbol{\gamma}}_2(s))]. \quad (30)$$

With the established coordinate system, we now consider the point spread function for the classical ‘‘azimuth’’ and ‘‘range’’ directions<sup>1</sup> separately. In the ‘‘azimuth’’ direction, we take the points  $\mathbf{x} = [a, x_2, 0]$  and  $\mathbf{z} = [a, z_2, 0]$ , and the point spread function integration simplifies to

$$K(\mathbf{x}, \mathbf{z}) = \int e^{i(x_2 - z_2)\xi_2} d\xi_2, \quad (31)$$

where

$$\begin{aligned} \xi_2 &= \frac{\omega}{c_0} \left[ \frac{x_2}{|\mathbf{x} - \boldsymbol{\gamma}_1(s)|} - \frac{x_2 - s}{|\mathbf{x} - \boldsymbol{\gamma}_2(s)|} \right] \\ &\approx \frac{\omega s}{c_0 R}, \end{aligned} \quad (32)$$

where we assume  $R = |\mathbf{x} - \boldsymbol{\gamma}_1(s)| \approx |\mathbf{x} - \boldsymbol{\gamma}_2(s)|$  is the range from the receivers to the target. The limits of integration are

<sup>1</sup>The classical notions of azimuth and range are no longer meaningful for the hitchhiker modality since the underlying manifold is not a circle, but a hyperbola. In classical monostatic SAR configuration with flat topography, where the underlying manifold is a circle,  $\boldsymbol{\xi}$  vector is aligned with the radius of the circle. This is not the case for the  $\boldsymbol{\xi}$  vector associated with the hitchhiker modality. Nevertheless, we use these specific directions so that the analysis can be understood in familiar terms.

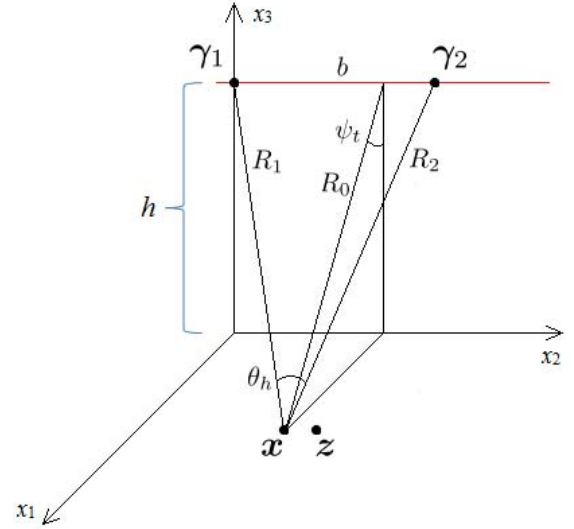


Fig. 3. Imaging geometry for determining resolution.  $\boldsymbol{\gamma}_1$  is the location of a stationary receiver, and  $\boldsymbol{\gamma}_2$  is the trajectory of a moving receiver traveling along the  $x_2$  direction, both at a height of  $h$ .

then  $[-\frac{\omega s_1}{R c_0}, \frac{\omega s_1}{R c_0}]$ , and the point spread function in the azimuth direction becomes

$$K(x_2, z_2) \propto \text{sinc} \left[ (x_2 - z_2) \frac{\omega s_1}{c_0 R} \right]. \quad (33)$$

This point spread function has a peak-to-null resolution of  $\frac{\pi c_0 R}{\omega s_1} = \frac{R \lambda}{2 s_1}$ . The antenna beamwidth, however, is proportional to  $2 R \lambda / L$ , where  $L$  is the size of the antenna, so the resolution becomes

$$\frac{R \lambda}{2 s_1} \cdot \frac{L}{2 R \lambda} = \frac{L}{4 s_1} \quad (34)$$

and we see that resolution becomes solely a function of the synthetic aperture length  $s_1$ .

In the ‘‘range’’ direction, we take the points  $\mathbf{x} = [x_1, a, 0]$  and  $\mathbf{z} = [z_1, a, 0]$ , and the point spread function integration simplifies to

$$K(\mathbf{x}, \mathbf{z}) = \int e^{i(x_1 - z_1)\xi_1} d\xi_1, \quad (35)$$

where

$$\begin{aligned} \xi_1 &= \frac{\omega}{c_0} \left[ \frac{x_1}{|\mathbf{x} - \boldsymbol{\gamma}_1(s)|} - \frac{x_1}{|\mathbf{x} - \boldsymbol{\gamma}_2(s)|} \right] \\ &= \frac{\omega}{c_0} \sin \psi_t \cos \theta_b \sin \theta_h \end{aligned} \quad (36)$$

where  $\theta_b$  is the angle between the synthetic aperture and the first antenna look direction,  $\theta_h$  is the hitchhiker angle, and  $\psi_t$  is the elevation angle between the synthetic aperture and target, as shown in Fig. 3. This equation shows that the resolution in the range direction is determined primarily by the bandwidth of the transmitted waveform and the hitchhiker angle.

### C. Velocity Resolution

Our image formation method reconstructs position images for a discrete set of velocities in a given range. The sampling of the velocity range is limited by the velocity resolution

TABLE II  
TABLE OF VELOCITY RESOLUTION PARAMETERS

Parameter	Increase ( $\uparrow$ )	Resolution
Transmitted waveform bandwidth $f = \omega/2\pi$	$\uparrow$	$\uparrow$
Aperture length $s$	$\uparrow$	$\uparrow$
Hitchhiker angle $\theta_h$	$\uparrow$	$\uparrow$
Number of receivers	$\uparrow$	$\uparrow$

available in the acquired data. To understand the velocity resolution and how finely the range of velocities can be discretized, we analyze the velocity bandwidth available in the data using the forward model (2).

We rewrite the forward model (2) in the following alternative form

$$\mathcal{F}[r](s, \tau) = \int e^{i\mathbf{s} \cdot \mathbf{v}} e^{-i\omega[\tau - R_{ij}(s, \mathbf{x})/c_0]} \times A_{ij}(\omega, s, \mathbf{x}, \mathbf{v}) r(\mathbf{x}, \mathbf{v}) d\mathbf{x} d\mathbf{v} d\omega \quad (37)$$

where

$$\boldsymbol{\zeta} = \omega s [(\widehat{\mathbf{x} - \boldsymbol{\gamma}_i}(s)) - (\widehat{\mathbf{x} - \boldsymbol{\gamma}_j}(s))]. \quad (38)$$

We can now interpret  $\boldsymbol{\zeta}$  as the Fourier vector associated with the velocity of the scatterer located at  $\mathbf{x}$  at  $s = 0$ . In an analogous fashion to the  $\boldsymbol{\xi}$  vector in Equation (14), the  $\boldsymbol{\zeta}$  vector provides information about the resolution in the velocity space. Directional diversity, as well as the length of this vector, determine the velocity resolution available in the correlated data  $d_{ij}$ . There are three factors that determine the length and direction of  $\boldsymbol{\zeta}$ : the bandwidth of the transmitted waveform, the synthetic aperture length and hitchhiker look direction. All three factors agree with intuition. Larger transmitted waveform bandwidth implies shorter processing windows and hence finer acquisition of range variation from one processing window to another which translates into finer velocity information. Longer aperture length shows that more information about the target velocity can be acquired as the target moves farther away from its original location. Both of these parameters are scaled by the length of the hitchhiker look direction vector, which is maximized when the hitchhiker angle is  $180^\circ$ .

Similarly to the position error simulation, the angle of the  $\boldsymbol{\zeta}$  vector is determined by the hitchhiker look direction. Therefore, angular diversity in the  $\boldsymbol{\zeta}$  vector is improved by a large synthetic aperture length as well as multiple receiver pairs. These parameters are summarized in Table II.

#### IV. POSITION ERROR ANALYSIS IN RECONSTRUCTED IMAGES DUE TO INCORRECT VELOCITY

This section addresses the following important questions in passive SAR imaging of moving targets:

- 1) Passive SAR images of moving targets reconstructed under the stationary scene assumption contain positioning errors or smearing artifacts. Given the imaging geometry and target velocities, can we develop a theory to analyze and predict the positioning errors in SAR images? In return, such a theory can be utilized to determine target velocities.

- 2) We have shown in Part 1 [12] of our study that radiance images can be focused if the target velocities are known a priori or correctly estimated. Based on this result, we reconstruct radiance images for a set of hypothesized velocities and select the velocity that yields the best focus. However, both the discretized hypothesized velocity and the estimated velocity may not be identically equal to the true velocity of the targets. Thus, if the hypothesized or estimated target velocity deviates from the true velocity, what would be the positioning errors in radiance images? Furthermore, if a small error is made in the hypothesized or estimated target velocity, is the resulting positioning error small? In other words, is our method of reconstructing radiance (position) images robust with respect to error in velocity estimation?

To analyze and predict positioning errors due to moving targets or erroneous velocity estimation, we use microlocal analysis, specifically the results that explain how the edges or scatterer locations in the scene are propagated into the reconstructed image by the filtered backprojection operator (8).

The concept of canonical relations explains how an FIO propagates scene information to acquired data for a given imaging geometry and other parameters. The Hörmander-Sato theorem, which relies on the composition of the canonical relations [14], [15], describes how the information acquired from the scene is propagated into the reconstructed image via the composition of the two FIOs defined as forward and inverse maps.

Recall that from Part 1 [12] that the phase of the image fidelity operator  $\mathcal{KF}$  is given by

$$\begin{aligned} \Phi_{ij}^{(\mathbf{v}, \mathbf{v}_h)}(\omega, s, \mathbf{x}', \mathbf{x}) &= \varphi_{ij}(\mathbf{x}', \mathbf{v}_h, s) - \varphi_{ij}(\mathbf{x}, \mathbf{v}, s) \\ &= \frac{\omega}{c_0} [R_{ij}(\mathbf{x}', s) + B_{ij}(\mathbf{x}', \mathbf{v}_h, s) \\ &\quad - R_{ij}(\mathbf{x}, s) - B_{ij}(\mathbf{x}, \mathbf{v}, s)] \quad (39) \end{aligned}$$

where  $\mathbf{x}$  and  $\mathbf{v}$  are scene parameters or target position and velocity and  $\mathbf{x}'$  is the image parameter and  $\mathbf{v}_h$  is the hypothesized velocity for which the FBP image is formed. The Hörmander-Sato theorem tells us that a scatterer located at  $\mathbf{x}$  at  $s = 0$  moving with velocity  $\mathbf{v}_x$  is formed at locations  $\mathbf{x}'$  moving with velocity  $\mathbf{v}_h$  that satisfy the two equations

$$\partial_\omega \Phi_{ij}^{(\mathbf{v}, \mathbf{v}_h)}(\omega, s, \mathbf{x}', \mathbf{x}) = \varphi_{ij}(\mathbf{x}', \mathbf{v}_h, s) - \varphi_{ij}(\mathbf{x}, \mathbf{v}, s) = 0, \quad (40)$$

$$\partial_s \Phi_{ij}^{(\mathbf{v}, \mathbf{v}_h)}(\omega, s, \mathbf{x}', \mathbf{x}) = \dot{\varphi}_{ij}(\mathbf{x}', \mathbf{v}_h, s) - \dot{\varphi}_{ij}(\mathbf{x}, \mathbf{v}, s) = 0, \quad (41)$$

where  $\dot{\varphi}$  denotes the derivative of  $\varphi$  with respect to  $s$ . Clearly, one of the solutions of (40) and (41) is  $\mathbf{x}' = \mathbf{x}$  when  $\mathbf{v}_h = \mathbf{v}_x$ , which tells us that the scatterer is reconstructed at the correct position (and orientation) whenever the hypothesized velocity of the scatterer is equal to its true velocity. Now let us assume that an error is made in the hypothesized velocity, i.e.,  $\mathbf{v}_h$  used in image reconstruction does not equal  $\mathbf{v} = \mathbf{v}_x$  but rather

$$\mathbf{v}_\epsilon = \mathbf{v}_x + \epsilon \Delta \mathbf{v}, \quad (42)$$

where  $\epsilon \Delta \mathbf{v}$  is the error in hypothesized velocity and  $\epsilon$  is a small constant. The backprojection operator then maps the scatterer to an erroneous location  $\mathbf{x}' + \Delta \mathbf{x}'$  in the reconstructed

image that satisfies the conditions

$$\varphi_{ij}(\mathbf{x}' + \Delta\mathbf{x}', \mathbf{v} + \epsilon\Delta\mathbf{v}, s) - \varphi_{ij}(\mathbf{x}, \mathbf{v}, s) = 0, \quad (43)$$

$$\dot{\varphi}_{ij}(\mathbf{x}' + \Delta\mathbf{x}', \mathbf{v} + \epsilon\Delta\mathbf{v}, s) - \dot{\varphi}_{ij}(\mathbf{x}, \mathbf{v}, s) = 0, \quad (44)$$

where  $\Delta\mathbf{x}'$  denotes the positioning error due to velocity error  $\epsilon\Delta\mathbf{v}$ . Our objective is to determine an approximate expression for  $\Delta\mathbf{x}'$  in terms of the velocity error  $\epsilon\Delta\mathbf{v}$ .

By making a Taylor series approximation around  $\epsilon = 0$  for each equation, we find the following relationships for position error:

$$\Xi_{ij}(\mathbf{x}', \mathbf{v}, s) \cdot \Delta\mathbf{x}' = -\mathbf{L}_{ij}(\mathbf{x}', s) \cdot \Delta\mathbf{v}s\epsilon, \quad (45)$$

$$-\dot{\Xi}_{ij}(\mathbf{x}', \mathbf{v}, s) \cdot \Delta\mathbf{x}' = \mathbf{L}_{ij}(\mathbf{x}', s) \cdot \Delta\mathbf{v}\epsilon - \dot{\mathbf{L}}_{ij}(\mathbf{x}', s) \cdot \Delta\mathbf{v}s\epsilon, \quad (46)$$

where  $\mathbf{L}_{ij}(\mathbf{x}', s)$  is the hitchhiker look direction

$$\mathbf{L}_{ij}(\mathbf{x}', s) = [(\mathbf{x}' - \widehat{\boldsymbol{\gamma}}_i(s)) - (\mathbf{x}' - \widehat{\boldsymbol{\gamma}}_j(s))], \quad (47)$$

and  $\dot{\mathbf{L}}_{ij}(\mathbf{x}', s)$  represents the derivative of  $\mathbf{L}_{ij}(\mathbf{x}', s)$  with respect to  $s$ . It is given by

$$\dot{\mathbf{L}}_{ij}(\mathbf{x}', s) = \frac{\dot{\boldsymbol{\gamma}}_i^\perp(s)}{|\mathbf{x}' - \widehat{\boldsymbol{\gamma}}_i(s)|} - \frac{\dot{\boldsymbol{\gamma}}_j^\perp(s)}{|\mathbf{x}' - \widehat{\boldsymbol{\gamma}}_j(s)|}, \quad (48)$$

with

$$\dot{\boldsymbol{\gamma}}_i^\perp(s) = \dot{\boldsymbol{\gamma}}_i(s) - (\mathbf{x}' - \widehat{\boldsymbol{\gamma}}_i(s))[\dot{\boldsymbol{\gamma}}_i(s) \cdot (\mathbf{x}' - \widehat{\boldsymbol{\gamma}}_i(s))], \quad (49)$$

$$\dot{\boldsymbol{\gamma}}_j^\perp(s) = \dot{\boldsymbol{\gamma}}_j(s) - (\mathbf{x}' - \widehat{\boldsymbol{\gamma}}_j(s))[\dot{\boldsymbol{\gamma}}_j(s) \cdot (\mathbf{x}' - \widehat{\boldsymbol{\gamma}}_j(s))]. \quad (50)$$

See Appendix A for the derivation of (45) and (46).

Note that  $\dot{\boldsymbol{\gamma}}_i^\perp(s)$  represents the component of the velocity of the  $i$ th receiver in the direction perpendicular to the look direction of the receiver.

Equations (45) and (46) represent the amount of position error in the direction of two different vectors:  $\Xi_{ij}$  and  $\dot{\Xi}_{ij}$ . To see the true error magnitude in each direction, we normalize the two equations with respect to the magnitude of these vectors and obtain

$$\widehat{\Xi}_{ij} \cdot \Delta\mathbf{x}' = \frac{-1}{|\Xi_{ij}|} \mathbf{L}_{ij}(\mathbf{x}', s) \cdot \Delta\mathbf{v}s\epsilon, \quad (51)$$

$$\widehat{\dot{\Xi}}_{ij} \cdot \Delta\mathbf{x}' = \frac{-1}{|\dot{\Xi}_{ij}|} [\mathbf{L}_{ij}(\mathbf{x}', s) \cdot \Delta\mathbf{v}\epsilon - \dot{\mathbf{L}}_{ij}(\mathbf{x}', s) \cdot \Delta\mathbf{v}s\epsilon]. \quad (52)$$

It is important to note that the magnitude factor  $|\dot{\Xi}_{ij}|$  contains the range terms in the denominator. When we normalize the second equation and divide by this magnitude, the range terms multiply the error, which can result in a significant quantity. To understand this error relationship further, we analyze the simplified case of a short synthetic aperture viewing a small scene. Additionally, we assume the antenna ranges are of the same order:  $|\mathbf{x}' - \widehat{\boldsymbol{\gamma}}_i(s)| \approx |\mathbf{x}' - \widehat{\boldsymbol{\gamma}}_j(s)|$ . Under these assumptions, we have the relationships

$$\mathbf{L}_{ij} \perp [\dot{\boldsymbol{\gamma}}_i^\perp(s) - \dot{\boldsymbol{\gamma}}_j^\perp(s)], \quad (53)$$

$$\mathbf{L}_{ij} \approx \Xi_{ij}. \quad (54)$$

Thus, the position errors in (51) and (52) further simplify to

$$\widehat{\mathbf{L}}_{ij} \cdot \Delta\mathbf{x}' = -\widehat{\mathbf{L}}_{ij}(\mathbf{x}', s) \cdot \Delta\mathbf{v}s\epsilon, \quad (55)$$

$$\widehat{\dot{\mathbf{L}}}_{ij} \cdot \Delta\mathbf{x}' = \frac{-1}{|\dot{\Xi}_{ij}|} [\mathbf{L}_{ij}(\mathbf{x}', s) \cdot \Delta\mathbf{v}\epsilon - \dot{\mathbf{L}}_{ij}(\mathbf{x}', s) \cdot \Delta\mathbf{v}s\epsilon]. \quad (56)$$

TABLE III

TABLE OF POSITION AND VELOCITY ERROR RELATIONSHIPS

Case	Error in $\mathbf{L}_{ij}$	Error in $\dot{\mathbf{L}}_{ij}$
Velocity error perpendicular to look direction ( $\Delta\mathbf{v} \perp \mathbf{L}_{ij}$ )	None	$\frac{1}{ \Xi_{ij} } \dot{\mathbf{L}}_{ij} \cdot \Delta\mathbf{v}s\epsilon$
Velocity error parallel to look direction ( $\Delta\mathbf{v} \parallel \mathbf{L}_{ij}$ )	$-\widehat{\mathbf{L}}_{ij} \cdot \Delta\mathbf{v}s\epsilon$	$\frac{-1}{ \dot{\Xi}_{ij} } \mathbf{L}_{ij} \cdot \Delta\mathbf{v}\epsilon$

We look at two extreme cases: the velocity error perpendicular to the hitchhiker look direction and the velocity error parallel to the hitchhiker look direction. In the case where the velocity error is perpendicular to the hitchhiker look direction,  $\Delta\mathbf{v} \perp \mathbf{L}_{ij}$ . Here, the first equation becomes zero and all of the position error is in the direction of  $\dot{\Xi}_{ij}$ , as shown in the second equation. In the second case, where  $\Delta\mathbf{v} \parallel \mathbf{L}_{ij}$ , we obtain a position error in both directions. This is because the first equation is only in the direction of  $\mathbf{L}_{ij}$ , while the second equation has both the hitchhiker look direction and perpendicular antenna velocity direction. These conclusions are summarized in Table III.

From the analysis presented in this section, we draw two important conclusions: 1. If a scene has moving targets and the backprojection image is reconstructed under the assumption that the scene is stationary, equations (51) and (52) quantify the smearing artifacts or positioning errors in the reconstructed image with  $\Delta\mathbf{v} = -\mathbf{v}_x$ , where  $\mathbf{v}_x$  corresponds to the target velocity at true position  $\mathbf{x}$ . 2. Equations (51) and (52) show that if the error in hypothesized velocity is in the order of  $\epsilon$ , then the positioning errors in the FBP images are also in the order of  $\epsilon$ . Hence, our image reconstruction method is robust. In the following section, we numerically validate the analysis and theory presented in this and previous sections.

## V. NUMERICAL SIMULATIONS

This section presents two sets of numerical simulations to demonstrate the different types of theoretical performance analysis presented in the previous sections. All of the simulations are performed with a square scene of size  $[512 \times 512]$  meters discretized into  $[128 \times 128]$  pixels, so that each pixel represents 4 square meters. The receiving antennas fly in a circular flight trajectory around the scene with a radius of 1.5 km, an altitude of 1 km, and a speed of 261 m/s. The number of receivers, distance traveled, and separation of receivers were all varied in order to demonstrate these individual effects on image resolution.

Since our image formation method is based on filtered backprojection onto iso-range curves, we need high resolution waveforms with large bandwidth. Some examples of waveforms applicable to our method would be wireless network signals (WiFi), digital video broadcasting terrestrial (DVB-T) signals, and WiMAX waveforms. These signals have bandwidths in the MHz range [9], [16]. The transmitter is a stationary tower located outside the circular flight trajectory at a distance of about 2.1 km from the center of the scene. The transmitter uses a rectangular pulse of various lengths to demonstrate the impact of signal bandwidth on

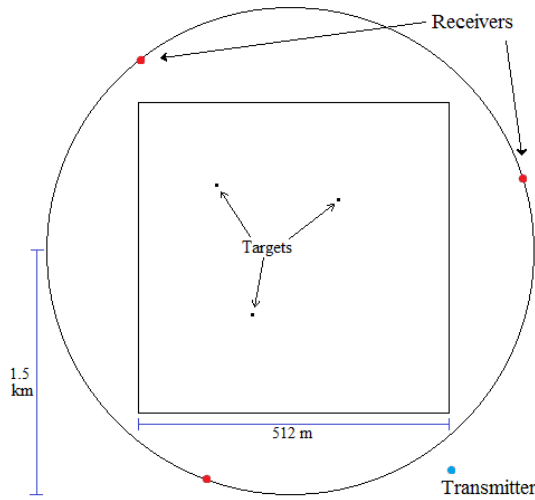


Fig. 4. Setup for the simulations. The receivers move in a circular trajectory with a radius of 1.5 km, while the transmitter is stationary outside of the scene. The scene size is  $[512 \times 512]$  m.

TABLE IV

BANDWIDTH OF THE SOURCES OF OPPORTUNITY VERSUS THE 3 dB WIDTH OF THE RECONSTRUCTED TARGET IN EACH DIRECTION

Bandwidth (MHz)	x-dir 3-dB Width (m)	y-dir 3-dB Width (m)
2.8	83.0	47.3
5.5	44.0	20.3
8.3	25.7	15.1
11.1	23.6	9.9
13.9	28.5	7.6
16.6	24.0	7.4

image resolution. A graphical illustration of this setup is shown in Fig. 4.

The data was generated by stepping through each slow-time and summing the signals scattered from each moving target in the scene. The velocity estimation and image reconstruction steps were performed as described in Section II. Note that the image reconstruction and velocity estimation procedure is based on the forward model, which is only an approximation to the method by which the data is collected. These performance analysis simulations used one target moving at 8 m/s. The target’s location is updated according to the slow-time variable, since we make the start-stop approximation in the model.

A. Resolution Analysis Simulations

In the first set of simulations, three different parameters are varied to show their increasing effect on image resolution for a correct hypothesized velocity. Transmitted wave bandwidth, synthetic aperture length, and hitchhiker angle all varied to demonstrate these dominant factors in image resolution.

First, we demonstrate the importance of bandwidth in image resolution. This was accomplished by changing the sampling frequency of the fast-time variable  $t$ , which is analogous to the transmitted pulse width and corresponds to bandwidth. The sampling frequency was varied in order to keep the bandwidth in a range around what one would find from available illuminating sources of opportunity, such as digital TV and WiMax signals [9], [16]. Bandwidth was varied from

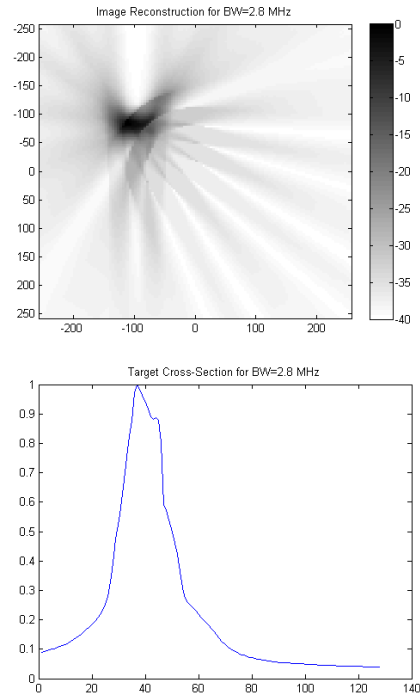


Fig. 5. Results for the case of bandwidth = 2.8 MHz. Top is the reconstructed image and bottom is the plot of the cross-section of the moving target.

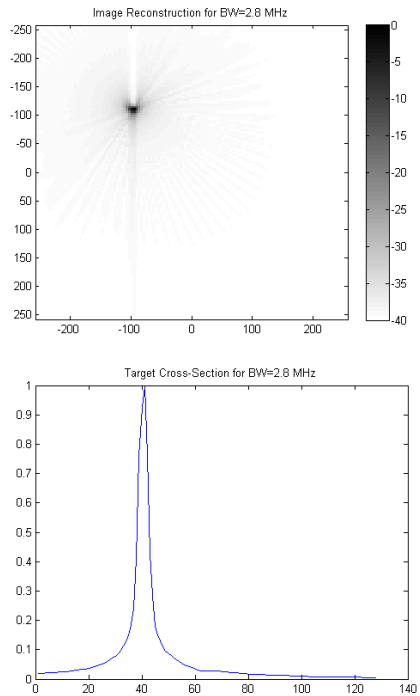


Fig. 6. Results for the case of bandwidth = 16.6 MHz. Top is the reconstructed image and bottom is the plot of the cross-section of the moving target.

about 3 to 17 MHz. The simulations were performed with two receivers flying over half of a circular synthetic aperture. Table IV shows the bandwidths used, as well as the 3-dB width of the cross-section of the reconstructed target in both the x-direction and y-direction. The decreasing target width indicates an increase in resolution, as we expect from an increasing bandwidth. Figs. 5 and 6 show the reconstructed images, along

TABLE V  
APERTURE LENGTH OF THE RECEIVING ANTENNAS VERSUS THE 3 dB  
WIDTH OF THE RECONSTRUCTED TARGET IN EACH DIRECTION

Aperture length (s)	x-dir 3-dB Width (m)	y-dir 3-dB Width (m)
2.1	52.6	4.2
4.2	26.9	4.3
6.3	17.6	4.3
8.5	16.0	4.4
10.6	14.8	4.8

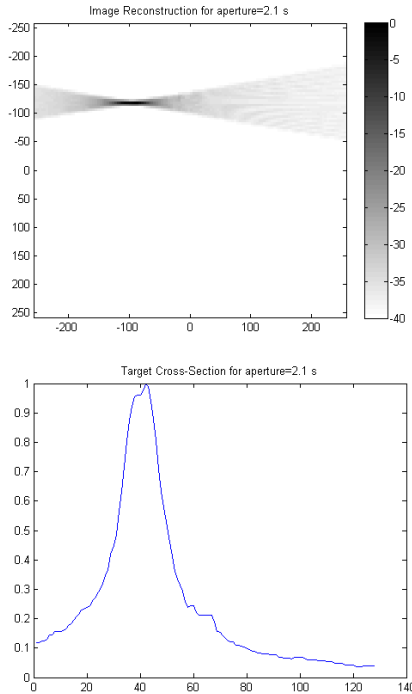


Fig. 7. Results for the case of aperture length = 4.2 s. Top is the reconstructed image and bottom is the plot of the cross-section of the moving target.

with the plot of the horizontal cross-sections for the lowest and highest bandwidth used, respectively.

In the second set of simulations, we vary the length of the synthetic aperture. Here, two receivers traversed the circular trajectory separated by a phase of  $180^\circ$  for various amounts of time. The flight time was varied from 2.1 seconds to 10.6 seconds, corresponding to aperture lengths from about 548 m to 2767 m, and the corresponding target cross-section widths are shown in Table V. Here we can see that the cross-range resolution (the x-direction in this scenario) is greatly improved by the increasing aperture length. Figs. 7 and 8 show the reconstructed images, along with the plot of the horizontal cross-sections for the shortest and longest apertures used, respectively.

The third parameter altered was the hitchhiker angle,  $\theta_h$ , discussed in Section III. This angle is an important property of the geometry because it directly determines the amount of data that is able to be recovered by the receivers. We vary the angle from  $10^\circ$  to  $70^\circ$  and show the corresponding results in Table VI. Figs. 9 and 10 show the reconstructed images along with the plot of the horizontal cross-sections for the smallest and largest angles used, respectively.

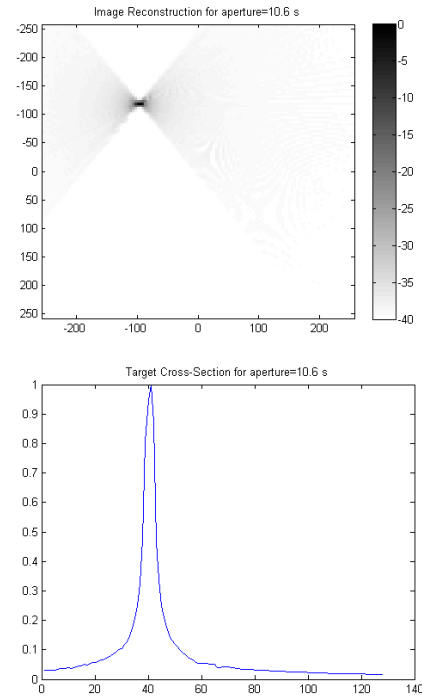


Fig. 8. Results for the case of aperture length = 21.2 s. Top is the reconstructed image and bottom is the plot of the cross-section of the moving target.

TABLE VI  
HITCHHIKER ANGLE BETWEEN THE RECEIVING ANTENNAS VERSUS THE  
3 dB WIDTH OF THE RECONSTRUCTED TARGET IN EACH DIRECTION

Hitchhiker angle	x-dir 3-dB Width (m)	y-dir 3-dB Width (m)
10	35.1	36.6
25	14.2	12.8
40	12.0	9.1
55	10.6	8.6
70	10.1	8.4

### B. Position Error Simulations

This section presents a set of simulations to illustrate the analysis done previously for error in position as a result of an incorrect hypothesized velocity. In each of two scenarios, a short aperture and single target were used to simulate the scenario of an approximately constant look direction and small scene, respectively. In each case, the length of the aperture was 1.1 s and the speed of the moving target was 28 m/s. Additionally, the hypothesized velocity was zero, so the error in velocity was equal in magnitude but opposite in direction to the target's true velocity.

Figs. 11 and 12 show results for the target traveling parallel and perpendicular, respectively, to the hitchhiker look direction for two antennas. The axes at the bottom-left of each image show these two directions, and the two markers show the true and reconstructed positions of the target. The dark, filled circle is the original location, and the empty circle is the reconstructed location.

Table VII summarizes the numerical results of these simulations. The table shows both the calculated and measured position error for the target in each direction of each simulation. The calculated error was obtained from equations

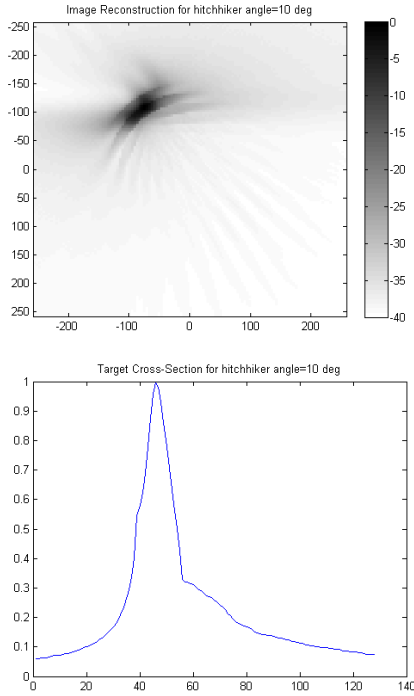


Fig. 9. Results for the case of hitchhiker angle = 10°. Top is the reconstructed image and bottom is the plot of the cross-section of the moving target.

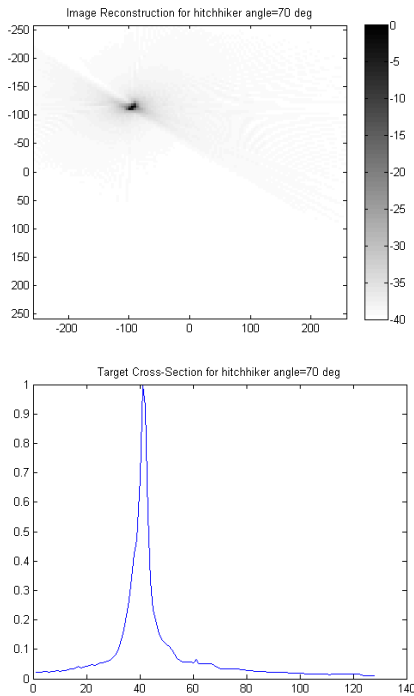


Fig. 10. Results for the case of hitchhiker angle = 70°. Top is the reconstructed image and bottom is the plot of the cross-section of the moving target.

(55) and (56), and the measured error was obtained from finding the difference between the true and reconstructed target positions. The first two rows show the error for the first simulation, where the target was moving up and towards the right, parallel to the look direction. In this situation, we obtain error in both directions, since each has a  $\mathbf{L} \cdot \Delta \mathbf{v}$  term.

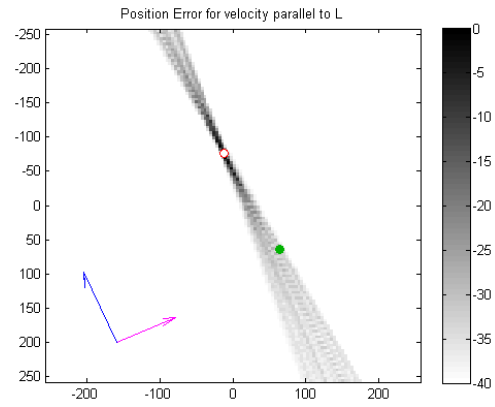


Fig. 11. Reconstructed image with a short aperture and target traveling parallel to the hitchhiker look direction. The solid circle is the original location of the target, and the hollow circle is the reconstructed location.

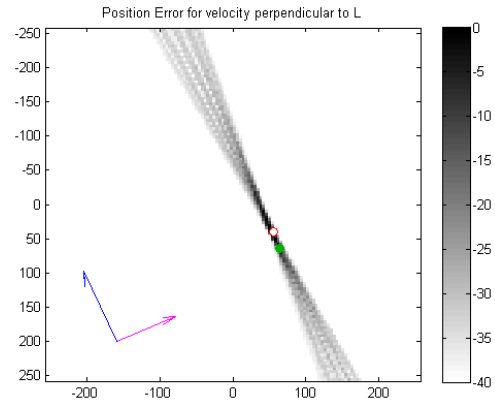


Fig. 12. Reconstructed image with a short aperture and target traveling perpendicular to the hitchhiker look direction. The solid circle is the original location of the target, and the hollow circle is the reconstructed location.

TABLE VII  
TABLE OF PREDICTED VS MEASURED POSITION ERROR

Setup	Direction	Predicted Error	Measured Error
$\Delta \mathbf{v} \parallel \mathbf{L}_{ij}$	$\mathbf{L}_{ij}$	16.0	13.0
$\Delta \mathbf{v} \parallel \mathbf{L}_{ij}$	$\hat{\mathbf{L}}_{ij}$	157.7	158.7
$\Delta \mathbf{v} \perp \mathbf{L}_{ij}$	$\mathbf{L}_{ij}$	1.3	2.4
$\Delta \mathbf{v} \perp \mathbf{L}_{ij}$	$\hat{\mathbf{L}}_{ij}$	29.2	25.2

The last two rows show the results for the second simulation, where the target velocity is approximately perpendicular to the look direction. In this scenario, the error in the look direction is almost zero since the only term that contributes to error in this direction is the dot product between orthogonal vectors. In reality, the error is slightly higher than zero, because only an approximately orthogonal velocity was used, as well as error contributions by numerical rounding and image resolution. An error in the  $\hat{\mathbf{L}}$  direction is still found, since this error has contributing terms in addition to the look direction.

Another set of simulations was performed with the same imaging geometry as in the previous scenario but with the speed of the target varying in order to show the linear relationship between velocity error and position error. The target was moving towards the right with a speed ranging

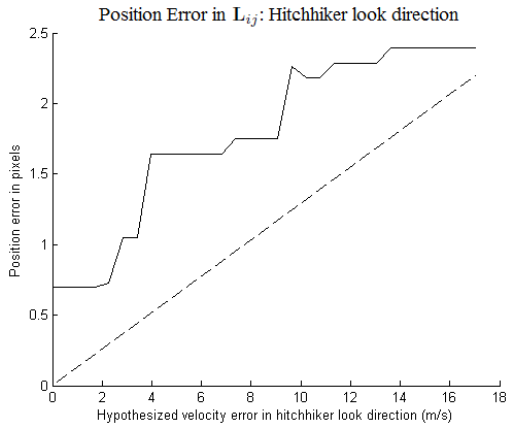


Fig. 13. Plot of the measured (solid) and predicted (dashed) position error along the hitchhiker look direction axis. The error in this direction is generally much smaller, but the increasing relationship between position and velocity error can still be seen here.

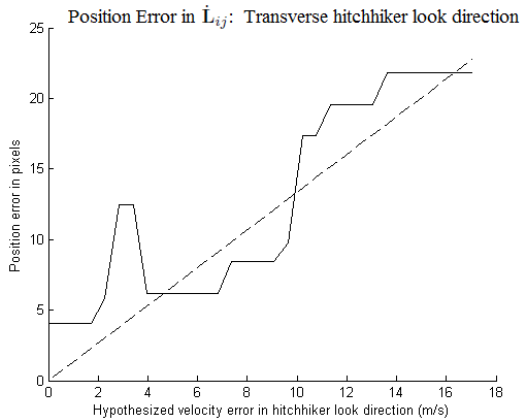


Fig. 14. Plot of the measured (solid) and predicted (dashed) position error along the axis of the time derivative of the hitchhiker look direction. One can see from this plot that the position error tends to increase as the hypothesized velocity error increases, and low hypothesized velocity errors yield more accurate reconstructed target positioning.

from 0 to 17 m/s. The position error versus speed is plotted in the look direction,  $\hat{\mathbf{L}}_{ij}$ , in Fig. 13 and in the derivative of the look direction,  $\dot{\hat{\mathbf{L}}}_{ij}$ , in Fig. 14. The blue lines show the predicted error, computed from (55) and (56), and the red lines show the measured error. The variations and discrepancies between the predicted and measured errors arise mostly from two factors: the look direction is not constant over the flight trajectory (it must be approximated by the average look direction), and the position of the reconstructed target is estimated by simply extracting the brightest spot in the image. Nevertheless, these graphs clearly demonstrate the increasing nature of the position error as the speed of the target increases.

## VI. CONCLUSION

This paper provided a performance analysis of the image reconstruction and velocity estimation method presented in [12]. Specifically we analyzed the resolution in both position and velocity spaces as well as the smearing artifacts from moving targets. The method is an extension of the stationary

case investigated in [5]–[7], by collecting signals with a network of mobile, passive receivers. These signals are correlated, and filtered backprojection is used to reconstruct a series of images over a range of hypothesized velocities. Entropy is then used to analyze smearing and choose the focused images with the estimated velocity for each moving target. Performance analysis of this method allows us to identify important factors involved in optimizing the system for high image resolution and accurate velocity estimation.

We began with a quick overview of the important aspects of the algorithm detailed in the first part. Next, a detailed resolution analysis was performed by looking at the form of the data from the forward model. Assuming a correctly hypothesized velocity, the image resolution was determined by looking at the bandwidth of the forward operator. Factors such as signal bandwidth, hitchhiker angle, number of receivers, and scene distance were identified as either contributing positively or negatively toward image resolution. Similarly for velocity resolution, the Fourier vector associated with velocity was analyzed to determine which factors increase or decrease the bandwidth in the velocity dimension of the data. Signal bandwidth, aperture length, and hitchhiker angle all contribute positively toward the velocity resolution. The angular span of the velocity Fourier vectors is increased with a large synthetic aperture or multiple receiver pairs. Increasing the number of receivers contributes to the angle diversity without increasing CPI, which is an important technique when imaging fast-maneuvering targets. The second major area of analysis involved the position error incurred when the hypothesized velocity is not equal to the true velocity. Simplifications were made to then split the error into two components: one in the hitchhiker look direction and the other in its perpendicular direction. We finally illustrated these results via numerical simulations.

Although the goal for this performance analysis was to analyze how imaging parameters affect position and velocity resolution as well as the positioning errors of moving targets, the method is applicable in the presence of additive white Gaussian noise. Under the assumption that the scene reflectivity and additive measurement noise are statistically uncorrelated and the additive measurement noise is zero-mean, then the cross-receiver correlation step yields a new random process (a new additive noise) that is a zero-mean and statistically uncorrelated in both slow-time and fast-time difference of arrival (the  $\tau$  variable). Under these conditions, the filtered-backprojection (FBP) method will provide the minimum mean squared error image, as shown in [17]. For colored noise, the filter can be modified to include prewhitening as we have shown in [18].

In future work, other aspects of performance analysis that are useful may be explored. An analysis that studies the variation in image entropy with respect to hypothesized velocity can be performed. The selection of images from image stack will determine the accuracy of velocity estimates as well as the degree of smearing, since the smearing is a function of incorrect velocity estimates. Therefore, an analysis of entropy, the metric of choice for final image selection, would also provide a valuable understanding to the problem. Other examples

are errors in receiver locations and phase coherence of the received signals. The algorithm and performance analysis both assume we have accurate locations for the mobile receivers at each slow-time; however, it is useful to analyze the error that occurs when there are small deviations between the true position and measured position of the antennas. Furthermore, the received signals at each receiver are combined coherently, so analyzing the effects of phase incoherence would be instructive as well. Additionally, the resolution analysis and position error analysis can be studied further to craft even more intelligent velocity estimation schemes. For example, the position error analysis can be used to describe various smearing artifacts in reconstructed images, which may then lead to an estimate of the velocity from the smears themselves. Finally, this work requires a relatively high bandwidth in order to accurately position the moving targets. However, since many of the available sources of opportunity transmit narrowband waveforms, we will investigate this case in future work.

#### APPENDIX A

##### DERIVATION OF THE POSITION ERROR

We now make the following Taylor series approximations about  $\epsilon = 0$  and write

$$\begin{aligned} \varphi_{ij}(\mathbf{x}' + \Delta\mathbf{x}', \mathbf{v} + \epsilon\Delta\mathbf{v}, s) &\approx \varphi_{ij}(\mathbf{x}', \mathbf{v}, s) \\ &+ \epsilon\partial_\epsilon\varphi_{ij}(\mathbf{x}', \mathbf{v} + \epsilon\Delta\mathbf{v}, s)|_{\epsilon=0} + \Delta\mathbf{x}' \cdot \nabla_{\mathbf{x}'}\varphi_{ij}(\mathbf{x}', \mathbf{v}, s), \end{aligned} \quad (57)$$

$$\begin{aligned} \dot{\varphi}_{ij}(\mathbf{x}' + \Delta\mathbf{x}', \mathbf{v} + \epsilon\Delta\mathbf{v}, s) &\approx \dot{\varphi}_{ij}(\mathbf{x}', \mathbf{v}, s) \\ &+ \epsilon\partial_\epsilon\dot{\varphi}_{ij}(\mathbf{x}', \mathbf{v} + \epsilon\Delta\mathbf{v}, s)|_{\epsilon=0} + \Delta\mathbf{x}' \cdot \nabla_{\mathbf{x}'}\dot{\varphi}_{ij}(\mathbf{x}', \mathbf{v}, s). \end{aligned} \quad (58)$$

Using equations (40), (41), (43), and (44) in (57) and (58) we have:

$$\epsilon\partial_\epsilon\varphi_{ij}(\mathbf{x}', \mathbf{v} + \epsilon\Delta\mathbf{v}, s)|_{\epsilon=0} + \Delta\mathbf{x}' \cdot \nabla_{\mathbf{x}'}\varphi_{ij}(\mathbf{x}', \mathbf{v}, s) = 0, \quad (59)$$

$$\epsilon\partial_\epsilon\dot{\varphi}_{ij}(\mathbf{x}', \mathbf{v} + \epsilon\Delta\mathbf{v}, s)|_{\epsilon=0} + \Delta\mathbf{x}' \cdot \nabla_{\mathbf{x}'}\dot{\varphi}_{ij}(\mathbf{x}', \mathbf{v}, s) = 0. \quad (60)$$

We now derive the relationship for the position and velocity errors for (59). The derivative with respect to  $\epsilon$  can be found as

$$\begin{aligned} \partial_\epsilon\varphi_{ij}(\mathbf{x}', \mathbf{v} + \epsilon\Delta\mathbf{v}, s)|_{\epsilon=0} &= \partial_\epsilon[R_{ij}(\mathbf{x}', s) \\ &+ \mathbf{L}_{ij}(\mathbf{x}', s) \cdot (\mathbf{v} + \epsilon\Delta\mathbf{v})s]|_{\epsilon=0} \\ &= \mathbf{L}_{ij}(\mathbf{x}', s) \cdot \Delta\mathbf{v}s \end{aligned} \quad (61)$$

where  $\mathbf{L}_{ij}(\mathbf{x}', s)$  is the hitchhiker look direction component in  $B_{ij}(\mathbf{x}', s)$ :

$$\mathbf{L}_{ij}(\mathbf{x}', s) = [(\widehat{\mathbf{x}' - \boldsymbol{\gamma}_i(s)} - \widehat{\mathbf{x}' - \boldsymbol{\gamma}_j(s)})]. \quad (62)$$

The gradient with respect to  $\mathbf{x}'$  is  $\mathbf{\Xi}_{ij}(\mathbf{x}', \mathbf{v}, s)$ , found in (16). Plugging these relationships back into (59), we obtain

$$\mathbf{L}_{ij}(\mathbf{x}', s) \cdot \Delta\mathbf{v}s\epsilon = -\mathbf{\Xi}_{ij}(\mathbf{x}', \mathbf{v}, s) \cdot \Delta\mathbf{x}'. \quad (63)$$

This equation describes one of the two sets of solutions for the position error. To fully understand the nature of this error, we must also solve the equation deriving the second set of conditions for the critical set of the phase, shown in (41).

We now derive the error relationship for (60). The first step is to start with the slow-time derivative of the phase  $\dot{\varphi}_{ij}(\mathbf{x}', \mathbf{v}, s)$  as

$$\begin{aligned} \dot{\varphi}_{ij}(\mathbf{x}', \mathbf{v}, s) &= \partial_s R_{ij}(\mathbf{x}', s) + \partial_s B_{ij}(\mathbf{x}', \mathbf{v}, s) \\ &= -\dot{\boldsymbol{\gamma}}_i(s) \cdot \widehat{(\mathbf{x}' - \boldsymbol{\gamma}_i(s))} + \dot{\boldsymbol{\gamma}}_j(s) \cdot \widehat{(\mathbf{x}' - \boldsymbol{\gamma}_j(s))} \\ &\quad + \frac{1}{|\mathbf{x}' - \boldsymbol{\gamma}_i(s)|} [(\mathbf{x}' - \boldsymbol{\gamma}_i(s)) \cdot \mathbf{v} - \dot{\boldsymbol{\gamma}}_i(s) \cdot \mathbf{v}s \\ &\quad - ((\mathbf{x}' - \boldsymbol{\gamma}_i(s)) \cdot \mathbf{v}s)(-\dot{\boldsymbol{\gamma}}_i(s) \cdot \widehat{(\mathbf{x}' - \boldsymbol{\gamma}_i(s))})] \\ &\quad - \frac{1}{|\mathbf{x}' - \boldsymbol{\gamma}_j(s)|} [(\mathbf{x}' - \boldsymbol{\gamma}_j(s)) \cdot \mathbf{v} - \dot{\boldsymbol{\gamma}}_j(s) \cdot \mathbf{v}s \\ &\quad - ((\mathbf{x}' - \boldsymbol{\gamma}_j(s)) \cdot \mathbf{v}s)(-\dot{\boldsymbol{\gamma}}_j(s) \cdot \widehat{(\mathbf{x}' - \boldsymbol{\gamma}_j(s))})] \\ &= (\widehat{(\mathbf{x}' - \boldsymbol{\gamma}_i(s))} \cdot (\mathbf{v} - \dot{\boldsymbol{\gamma}}_i(s)) - \widehat{(\mathbf{x}' - \boldsymbol{\gamma}_j(s))} \cdot (\mathbf{v} - \dot{\boldsymbol{\gamma}}_j(s)) \\ &\quad + \frac{-\dot{\boldsymbol{\gamma}}_i(s) \cdot \mathbf{v}s - ((\mathbf{x}' - \boldsymbol{\gamma}_i(s)) \cdot \mathbf{v}s)(-\dot{\boldsymbol{\gamma}}_i(s) \cdot \widehat{(\mathbf{x}' - \boldsymbol{\gamma}_i(s))})}{|\mathbf{x}' - \boldsymbol{\gamma}_i(s)|} \\ &\quad - \frac{-\dot{\boldsymbol{\gamma}}_j(s) \cdot \mathbf{v}s - ((\mathbf{x}' - \boldsymbol{\gamma}_j(s)) \cdot \mathbf{v}s)(-\dot{\boldsymbol{\gamma}}_j(s) \cdot \widehat{(\mathbf{x}' - \boldsymbol{\gamma}_j(s))})}{|\mathbf{x}' - \boldsymbol{\gamma}_j(s)|}) \end{aligned} \quad (64)$$

The next step is to find the derivative with respect to  $\epsilon$ ,  $\partial_\epsilon\dot{\varphi}_{ij}(\mathbf{x}', \mathbf{v} + \epsilon\Delta\mathbf{v}, s)$ :

$$\begin{aligned} \partial_\epsilon\dot{\varphi}_{ij}(\mathbf{x}', \mathbf{v} + \epsilon\Delta\mathbf{v}, s) &= (\widehat{(\mathbf{x}' - \boldsymbol{\gamma}_i(s))} \cdot \Delta\mathbf{v} - \widehat{(\mathbf{x}' - \boldsymbol{\gamma}_j(s))} \cdot \Delta\mathbf{v} \\ &\quad - \frac{\dot{\boldsymbol{\gamma}}_i(s) \cdot \Delta\mathbf{v}s + ((\mathbf{x}' - \boldsymbol{\gamma}_i(s)) \cdot \Delta\mathbf{v}s)(-\dot{\boldsymbol{\gamma}}_i(s) \cdot \widehat{(\mathbf{x}' - \boldsymbol{\gamma}_i(s))})}{|\mathbf{x}' - \boldsymbol{\gamma}_i(s)|} \\ &\quad + \frac{\dot{\boldsymbol{\gamma}}_j(s) \cdot \Delta\mathbf{v}s + ((\mathbf{x}' - \boldsymbol{\gamma}_j(s)) \cdot \Delta\mathbf{v}s)(-\dot{\boldsymbol{\gamma}}_j(s) \cdot \widehat{(\mathbf{x}' - \boldsymbol{\gamma}_j(s))})}{|\mathbf{x}' - \boldsymbol{\gamma}_j(s)|}) \end{aligned} \quad (65)$$

and the gradient with respect to  $\mathbf{x}'$ ,  $\nabla_{\mathbf{x}'}\dot{\varphi}_{ij}(\mathbf{x}', \mathbf{v}, s)$ :

$$\begin{aligned} \nabla_{\mathbf{x}'}\dot{\varphi}_{ij}(\mathbf{x}', \mathbf{v}, s) &= \nabla_{\mathbf{x}'}\partial_s\varphi_{ij}(\mathbf{x}', \mathbf{v}, s) \\ &= \mathbf{\Xi}_{ij}(\mathbf{x}', \mathbf{v}, s). \end{aligned} \quad (66)$$

The relationship can now be written as

$$\begin{aligned} \epsilon\partial_\epsilon\dot{\varphi}_{ij}(\mathbf{x}', \mathbf{v} + \epsilon\Delta\mathbf{v}, s) &= -\nabla_{\mathbf{x}'}\dot{\varphi}_{ij}(\mathbf{x}', \mathbf{v}, s) \cdot \Delta\mathbf{x}' \\ &\quad - \mathbf{\Xi}_{ij}(\mathbf{x}', \mathbf{v}, s) \cdot \Delta\mathbf{x}' = \mathbf{L}_{ij}(\mathbf{x}', s) \cdot \Delta\mathbf{v}\epsilon \\ &\quad - \frac{\dot{\boldsymbol{\gamma}}_i(s) \cdot \Delta\mathbf{v}s\epsilon + ((\mathbf{x}' - \boldsymbol{\gamma}_i(s)) \cdot \Delta\mathbf{v}s\epsilon)(-\dot{\boldsymbol{\gamma}}_i(s) \cdot \widehat{(\mathbf{x}' - \boldsymbol{\gamma}_i(s))})}{|\mathbf{x}' - \boldsymbol{\gamma}_i(s)|} \\ &\quad + \frac{\dot{\boldsymbol{\gamma}}_j(s) \cdot \Delta\mathbf{v}s\epsilon + ((\mathbf{x}' - \boldsymbol{\gamma}_j(s)) \cdot \Delta\mathbf{v}s\epsilon)(-\dot{\boldsymbol{\gamma}}_j(s) \cdot \widehat{(\mathbf{x}' - \boldsymbol{\gamma}_j(s))})}{|\mathbf{x}' - \boldsymbol{\gamma}_j(s)|} \\ &= \mathbf{L}_{ij}(\mathbf{x}', s) \cdot \Delta\mathbf{v}\epsilon - \left[ \frac{\dot{\boldsymbol{\gamma}}_i^\perp(s)}{|\mathbf{x}' - \boldsymbol{\gamma}_i(s)|} - \frac{\dot{\boldsymbol{\gamma}}_j^\perp(s)}{|\mathbf{x}' - \boldsymbol{\gamma}_j(s)|} \right] \cdot \Delta\mathbf{v}s\epsilon \\ &= \mathbf{L}_{ij}(\mathbf{x}', s) \cdot \Delta\mathbf{v}\epsilon - \dot{\mathbf{L}}_{ij}(\mathbf{x}', s) \cdot \Delta\mathbf{v}s\epsilon \end{aligned} \quad (67)$$

where  $\dot{\mathbf{L}}_{ij}(\mathbf{x}', s)$  is the hitchhiker look direction component in  $B_{ij}(\mathbf{x}', s)$ :

$$\dot{\mathbf{L}}_{ij}(\mathbf{x}', s) = [(\widehat{(\mathbf{x}' - \boldsymbol{\gamma}_i(s))} - \widehat{(\mathbf{x}' - \boldsymbol{\gamma}_j(s))})] \quad (69)$$

and

$$\dot{\boldsymbol{\gamma}}_i^\perp(s) = \dot{\boldsymbol{\gamma}}_i(s) - \widehat{(\mathbf{x}' - \boldsymbol{\gamma}_i(s))}[\dot{\boldsymbol{\gamma}}_i(s) \cdot \widehat{(\mathbf{x}' - \boldsymbol{\gamma}_i(s))}] \quad (70)$$

$$\dot{\boldsymbol{\gamma}}_j^\perp(s) = \dot{\boldsymbol{\gamma}}_j(s) - \widehat{(\mathbf{x}' - \boldsymbol{\gamma}_j(s))}[\dot{\boldsymbol{\gamma}}_j(s) \cdot \widehat{(\mathbf{x}' - \boldsymbol{\gamma}_j(s))}]. \quad (71)$$

## REFERENCES

- [1] J. Brown, K. Woodbridge, H. Griffiths, A. Stove, and S. Watts, "Passive bistatic radar experiments from an airborne platform," *IEEE Aerosp. Electron. Syst. Mag.*, vol. 27, no. 11, pp. 50–55, Nov. 2012.
- [2] B. Dawidowicz, P. Samczynski, M. Malanowski, J. Misiurewicz, and K. S. Kulpa, "Detection of moving targets with multichannel airborne passive radar," *IEEE Aerosp. Electron. Syst. Mag.*, vol. 27, no. 11, pp. 42–49, Nov. 2012.
- [3] P. Krysik and K. Kulpa, "The use of a GSM-based passive radar for sea target detection," in *Proc. IEEE 9th Eur. Radar Conf. (EuRAD)*, Oct./Nov. 2012, pp. 142–145.
- [4] M. M. Chitgarha, M. N. Majd, M. Radmard, and M. M. Nayebi, "Choosing the position of the receiver in a MISO passive radar system," in *Proc. IEEE 9th Eur. Radar Conf. (EuRAD)*, Oct./Nov. 2012, pp. 318–321.
- [5] C. E. Yarman and B. Yazıcı, "Synthetic aperture hitchhiker imaging," *IEEE Trans. Image Process.*, vol. 17, no. 11, pp. 2156–2173, Nov. 2008.
- [6] C. E. Yarman, L. Wang, and B. Yazıcı, "Doppler synthetic aperture hitchhiker imaging," *Inverse Probl.*, vol. 26, no. 6, p. 065006, 2010.
- [7] L. Wang, C. E. Yarman, and B. Yazıcı, "Doppler-hitchhiker: A novel passive synthetic aperture radar using ultranarrowband sources of opportunity," *IEEE Trans. Geosci. Remote Sens.*, vol. 49, no. 10, pp. 3521–3537, Oct. 2011.
- [8] L. Wang, I.-Y. Son, and B. Yazıcı, "Passive imaging using distributed apertures in multiple-scattering environments," *Inverse Probl.*, vol. 26, no. 6, p. 065002, 2010.
- [9] L. Wang and B. Yazıcı, "Passive imaging of moving targets using sparse distributed apertures," *SIAM J. Imag. Sci.*, vol. 5, no. 3, pp. 769–808, 2012.
- [10] J. E. Palmer and S. J. Searle, "Evaluation of adaptive filter algorithms for clutter cancellation in passive bistatic radar," in *Proc. IEEE Radar Conf. (RADAR)*, May 2012, pp. 493–498.
- [11] C. J. Coleman, R. A. Watson, and H. Yardley, "A practical bistatic passive radar system for use with DAB and DRM illuminators," in *Proc. IEEE Radar Conf. (RADAR)*, May 2008, pp. 1–6.
- [12] S. Wacks and B. Yazıcı, "Passive synthetic aperture hitchhiker imaging of ground moving targets—Part 1: Image formation and velocity estimation," *IEEE Trans. Image Process.*, vol. 23, no. 6, pp. 2487–2500, Jun. 2014.
- [13] A. F. Yegulalp, "Analysis of SAR image formation equations for stationary and moving targets," MIT Lincoln Laboratory, Lexington, MA, USA, Tech. Rep. TR-2001-074, 2002.
- [14] B. Yazıcı and V. Krishnan. (2010, Aug.). *Microlocal Analysis in Imaging*. [Online]. Available: [http://www.ecse.rpi.edu/~yazici/ICASSPTutorial/microlocal\\_ICASSP10.html](http://www.ecse.rpi.edu/~yazici/ICASSPTutorial/microlocal_ICASSP10.html), accessed on Aug. 3, 2013.
- [15] J. F. Treves, "Fourier integral operators," in *Introduction to Pseudodifferential and Fourier Integral Operators*, vol. 2. New York, NY, USA: Springer-Verlag, 1980.
- [16] H. D. Griffiths and C. J. Baker, "Passive coherent location radar systems. Part 1: Performance prediction," *IEE Proc., Radar, Sonar Navigat.*, vol. 152, no. 3, pp. 153–159, Jun. 2005.
- [17] K. Voccola, B. Yazıcı, M. Ferrara, and M. Cheney, "On the relationship between the generalized likelihood ratio test and backprojection for synthetic aperture radar imaging," *Proc. SPIE Defense, Security, Sens.*, vol. 7335, p. 73350I, May 2009.
- [18] B. Yazıcı, M. Cheney, and C. E. Yarman, "Synthetic-aperture inversion in the presence of noise and clutter," *Inverse Probl.*, vol. 22, no. 5, p. 1705, 2006.



**Steven Wacks** received the B.S. degree in electrical engineering and computer science and the Ph.D. degree in electrical engineering from the Rensselaer Polytechnic Institute, Troy, NY, USA, in 2010 and 2014, respectively.

He is currently with the MIT Lincoln Laboratory, Lexington, MA, USA. His research interests include radar, imaging, and signal processing.



**Birsen Yazıcı** received the B.S. degrees in electrical engineering and mathematics from Bogazici University, Istanbul, Turkey, in 1988, and the M.S. and Ph.D. degrees in mathematics and electrical engineering from Purdue University, West Lafayette, IN, USA, in 1990 and 1994, respectively. From 1994 to 2000, she was a Research Engineer with the General Electric Company Global Research Center, Schenectady, NY, USA. During her tenure in the industry, she worked on radar, transportation, industrial, and medical imaging systems. From 2001 to 2003, she was an Assistant Professor with the Department of Electrical and Computer Engineering, Drexel University, Philadelphia, PA, USA. In Fall 2003, she joined the Rensselaer Polytechnic Institute, Troy, NY, USA, where she is currently a Full Professor with the Department of Electrical, Computer and Systems Engineering and the Department of Biomedical Engineering.

Prof. Yazıcı's research interests span the areas of statistical signal processing, inverse problems in imaging, image reconstruction, biomedical optics, radar, and X-ray imaging. From 2008 to 2012, she was an Associate Editor of the IEEE TRANSACTIONS ON IMAGE PROCESSING. She currently serves as an Associate Editor of the *SIAM Journal on Imaging Science* and the IEEE TRANSACTIONS ON GEOSCIENCES AND REMOTE SENSING. She was a recipient of the Rensselaer Polytechnic Institute's 2007 and 2013 School of Engineering Research Excellence Awards. She holds 11 U.S. patents.